J. Mech. Phys. Solids 190 (2024) 105712

Contents lists available at ScienceDirect

Journal of the Mechanics and Physics of Solids

journal homepage: www.elsevier.com/locate/jmps

Mineral asperities reinforce nacre through interlocking and friction-like sliding

Hao Li [a], Kun Geng [a], Bingzhan Zhu [a], Qiang Zhang [a], Yi Wen [a], Zuoqi Zhang [a,b,*], Yanan Yuan [a,b,*], Huajian Gao [c,d]

[a] Department of Engineering Mechanics, School of Civil Engineering, Wuhan University, Wuhan, 430072, PR China
[b] Engineering Research Center on Building Examination and Reinforcement Technology (Ministry of Education), Wuhan University, Wuhan, 430071, PR China
[c] School of Mechanical and Aerospace Engineering, Nanyang Technological University, 639798, Singapore
[d] Institute of High Performance Computing, A*STAR, 138632, Singapore

ARTICLE INFO

Keywords:
Biological composites
Bionic composites
Microstructured interface
Mechanical interlocking
Sliding and friction

ABSTRACT

While the surface asperities of mineral platelets are widely believed to play important roles in stiffening, strengthening, and toughening nacre, their effects have not been thoroughly investigated. Here, a computationally efficient bar-spring model is adopted to simulate, as platelets with multiple interfacial asperities slide over each other, the tensile force versus elongation behaviors as well as the effective mechanical properties such as modulus, strength, and work-to-fracture in nacre or nacre-like composites. The model employs an effective cohesive law derived from a micromechanical model based on the kinematic and deformation analysis of a single pair of contacting asperities to characterize the traction-separation relationship during the asperity interclimbing. Strikingly, we find that the mineral asperities and resulting interfacial roughness can elevate the composites' strength and toughness by up to 2–3 orders of magnitude through a combination of mechanical interlocking and multimodal friction-like mechanisms. Of particular interest is that the asperity-induced strengthening and toughening mechanisms are insensitive to the asperity shapes such as ellipse, hyperbolic cosine, cosine, and parabola. These findings may provide useful guidelines for developing advanced engineering composites with nacre-inspired interface designs.

1. Introduction

Natural load-bearing biological composites exhibit remarkable mechanical properties such as high stiffness, strength, toughness, reliability and durability in spite of inherently weak constituent materials (Tang et al., 2003; Meyers et al. 2008). In particular, nacre stands out as a prominent example of load-bearing biocomposites for achieving superior strength and toughness by combining brittle mineral platelets and soft polymer matrix through a "brick-and-mortar" microstructure (Currey and Sheppard 1977; Jackson et al. 1988; Sarikaya et al. 1989; Menig et al. 2000; Barthelat 2007). More than 95% volume fraction of nacre is aragonite, a type of calcium carbonate that has Young's modulus around 100 GPa but low fracture toughness ranging from 0.2 to 1 MPa·m$^{1/2}$ (Dashkovskiy et al. 2007; Alghamdi et al. 2018; Troncoso et al. 2020). The rest small volume fraction of biopolymers (mainly β-chitin) separates the

* Corresponding author.
E-mail addresses: zhang_zuoqi@whu.edu.cn (Z. Zhang), yuanyn@whu.edu.cn (Y. Yuan).

https://doi.org/10.1016/j.jmps.2024.105712
Received 6 January 2024; Received in revised form 1 May 2024; Accepted 28 May 2024
Available online 15 June 2024

aragonite into brick-like platelets and acts as a mortar matrix binding the platelets together. This microstructure allows nacre to achieve a comparable Young's modulus of approximately 60 GPa (Jackson et al. 1988) and a much higher fracture toughness of about 10 MPa·m$^{1/2}$ (Sarikaya et al. 1989) compared to aragonite (Jackson et al. 1990; Mayer 2006). The intriguing synergistic effects of nacre have sparked significant research interest in understanding the strengthening and toughening mechanisms associated with the brick-and-mortar microstructure (Gao et al. 2003; Ji and Gao 2004; Ji et al. 2004; Xu and Li 2011; Yu et al. 2020) and helping to develop nacre-inspired synthetic materials (Espinosa et al. 2009; Yao et al. 2014).

In the brick-and-mortar structure, the brittle-but-hard mineral platelets are arranged in a staggered fashion and primarily carry tensile force, while the soft-but-tough biopolymer matrix predominantly transfers load through shear deformation. This synergistic interplay capitalizes on their respective advantages, resulting in a simultaneous achievement of high stiffness, strength, and toughness. This mechanism has been elucidated through a series of theoretical models such as the tension-shear chain and related frameworks (Jager and Fratzl 2000; Gao et al. 2003; Ji and Gao 2004; Zhang et al. 2010; Bar-On and Wagner 2011). Several toughening mechanisms associated with the brick-and-mortar microstructure have been proposed, including crack blunting/branching/deflection, microcrack formation, platelets bridging, and platelets pull-out (Chen et al. 2010; Shao et al. 2012; Chen et al. 2015; Liang et al. 2020; Liu et al. 2020). Additionally, based on fracture mechanics, it has been demonstrated that the nanoscale thickness of mineral platelets leads to their strength approaching the theoretical limit, without the typical strength reduction caused by crack-like flaws at the macroscale (Gao et al. 2003). Furthermore, hierarchical structures in biological materials can effectively upscale their excellent mechanical performance from nano to macro (Gao 2006) through proper selection of the number of hierarchical levels, as well as the structural arrangement and characteristic size at each level of hierarchy (Zhang et al. 2011).

While the brick-and-mortar structure is important, it alone cannot ensure the extraordinary mechanical properties of nacre. This is evident from the mechanical performance of bioinspired composites that mimic the brick-and-mortar structure (Katti and Katti 2006). Multiple key structural features must work together to achieve the same level of performances in nacre (Chen et al. 2021). In particular, several sub-microscale structural features along the interfaces between neighboring mineral platelets have been identified as crucial contributors to the strengthening and toughening mechanism of nacre. For example, scanning electron micrographs reveal dovetail-like structures at the periphery of the mineral tablets (Sarikaya et al. 1989; Barthelat 2007; Barthelat and Espinosa 2007). The dovetail-like structures can bring into play a mechanical interlocking effect, resulting in a progressive, extensive and prolonged failure process (Katti and Katti 2006; Ghazlan et al. 2015). Moreover, in scenarios involving impact loads on nacre-like composites, the dovetail structure facilitates dynamic energy dissipation through greater plastic deformation in the polymer matrix (Zhang et al. 2022). Mineral bridges connecting overlapped mineral platelets, which represent another noteworthy structural feature of interest to both biologists and materials scientists, are believed to play a pivotal role in maintaining consistent crystallographic relationship of the mineral tablets (Schäffer et al. 1997; Checa et al. 2011) and ensuring mechanical integrity of the mineral framework (Song and Bai 2003; Song et al. 2003). Beyond the mineral bridges, a multitude of asperities are observed along the surfaces of mineral tablets in nacre, as evident in SEM images in Fig. 1a (Barthelat et al. 2006; Li et al. 2006; Meyers et al. 2008). The mineral bridges tend to undergo shear deformation and premature breakage when subjected to shear along the interface, and their remnants then function in a similar way as the mineral asperities. As overlapped mineral platelets slide against each other due to external loading, the asperities rise and climb up against their contacting counterparts along the inter-platelet interface (Song et al. 2008; Alghamdi et al. 2017; Alghamdi et al. 2018). The asperity climbing behavior results in notable strain hardening, lateral expansion, and energy dissipation

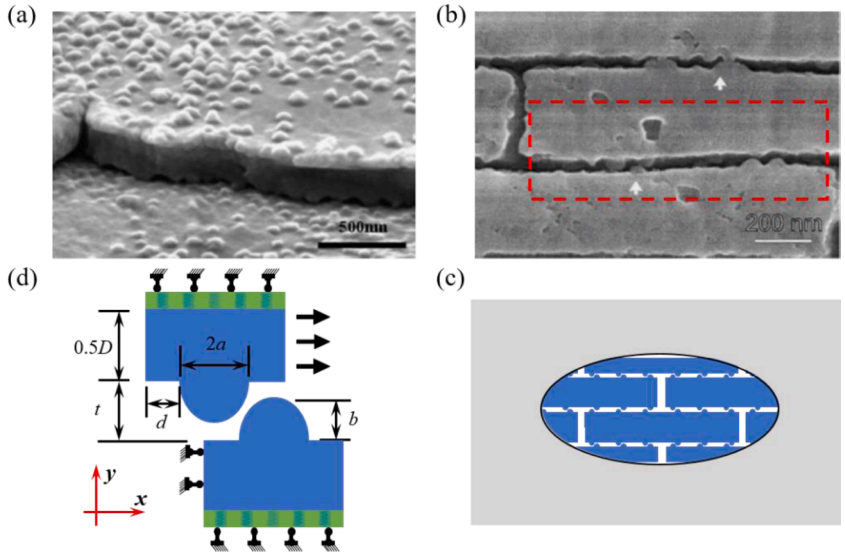

Fig. 1. (a) SEM images of mineral asperities on the platelets of nacre (Meyers et al. 2008); (b) Interaction of asperities along the overlapping interfaces between neighboring platelets (Wang et al. 2001); (c) The adopted two-dimensional model of asperity interaction, and (d) inter-climbing of a pair of asperities.

akin to friction. These factors can lead to inelastic deformation and enhanced fracture toughness (Evans et al. 2001; Wang et al. 2001; Barthelat and Espinosa 2007; Song et al. 2008). There has been significant interest in mimicking this secondary structural feature in the pursuit of nacre-inspired synthetic materials. For instance, Xia et al. successfully fabricated silica platelets with aragonite-like nano-asperities using a biomineralization approach. They then stacked the silica platelets and polyvinyl alcohol (PVA) alternately into a layered structure through a dip-coating method, resulting in nacre-like nanocomposites that possess both the primary (brick-and-mortar) and secondary (platelet surface asperities) structures (Xia et al. 2015). Subsequent mechanical tests demonstrated that the asperities on silica platelet surfaces significantly contribute to strain hardening, strength, and toughness. In spite of this and other more recent attempts to incorporate nacre-inspired submicroscale structural features into engineering composites for higher strength, toughness and fatigue resistance (Doineau et al. 2021; Tan et al. 2021; Zhang et al. 2021), the exact working mechanism of mineral asperities remains poorly understood.

With the aim to quantitatively understand the role of mineral asperities in the strengthening and toughening mechanisms of nacre, here we develop a theoretical modeling framework that accounts for the kinematics of inter-climbing interactions among asperities on opposite sliding interfaces. The remaining of this paper is organized as follows: Section 2 introduces the model; the associated strengthening and toughening behaviors are studied in Section 3; the main findings and conclusions are summarized in Section 4.

2. Model derivation

As shown in the SEM image in Fig. 1a, there are many nanoscale surface asperities on mineral tablets in nacre. These nano-asperities are topologically matched quite well prior to loading, as shown in the side-view SEM image of Fig. 1b (Wang et al. 2001), and the schematic illustration of Fig. 1c. To facilitate theoretical modeling, the asperities are assumed to be of the same shape and evenly distributed along the interface, as illustrated in Fig. 1c. Consider a two-dimensional representative volume element (RVE) containing a pair of interacting asperities subjected to elastic constraint from surrounding materials (represented by a cushion layer), as depicted in Fig. 1d, where a and b denote the half-width and height of each asperity, respectively, D the platelet thickness, t the platelet spacing and d the half-spacing between adjacent asperities on the same platelet surface. The aspect ratio (α) of an asperity can be defined as

$$\alpha = \frac{b}{a} \tag{1}$$

and the platelet volume ratio ϕ approximately as

$$\phi = \frac{D}{D+t} = \frac{1}{1+t/D} \tag{2}$$

where the volume of the asperities is considered negligible and hence not included.

As shown in Fig. 1d, under external loading, the overlapping mineral platelets would undergo sliding motion against each other, and consequently the asperities would come into closer contact. In Fig. 2a, we illustrate the initial contact configuration, where a fixed global coordinate frame x-y is defined with the horizontal axis x going through the center of the right asperity and the vertical axis y passing through the center of the left asperity. The abscissas of the right asperity center and the initial contacting point are denoted as

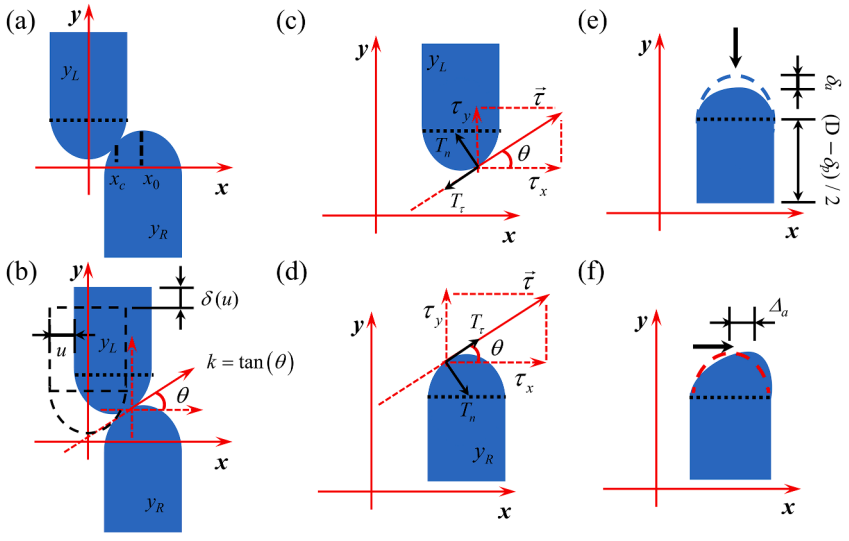

Fig. 2. Relative movement and contact between a pair of rigid asperities: (a) the initial contact, (b) the climbing stage, and the interaction forces on the left (c) and right (d) asperities. Asperity deformation: (e) axial compression, and (f) transverse bending.

x_0 and x_c, respectively. For simplicity, we consider half elliptical profile functions for the left (L) and right (R) asperities (Fig. 2a):

$$\begin{cases} y_L = -b\sqrt{1-\dfrac{x^2}{a^2}} + t \\ y_R = b\sqrt{1-\dfrac{(x-x_0)^2}{a^2}} \end{cases} \tag{3}$$

The lengths of semi-axes a and b correspond respectively to the asperity half-span and height in Fig. 1d. Note that our model can be easily extended to other asperity profiles and the results for several other asperity profiles will be discussed in Section 3. The asperity profiles considered in the present study are all smooth, since the asperity shapes in Figs. 1a and 1b all look like smooth bumps. The difference function

$$g(x) = y_L(x) - y_R(x) \tag{4}$$

defines the vertical gap between the two asperities. The condition for contact during the climbing process is

$$\begin{cases} g(x) = 0 \\ \dfrac{\partial g(x)}{\partial x} = 0 \end{cases} \tag{5}$$

Solving the above equations yields

$$\begin{cases} x_0 = 2a\sqrt{1-\dfrac{t^2}{4b^2}} \\ x_c = \dfrac{x_0}{2} \end{cases} \tag{6}$$

for the initial contact shown in Fig. 2a.

Fig. 2b shows an instantaneous configuration in the process of asperity climbing. For simplicity, the right asperity is assumed to be stationary, and the displacements of the left asperity in the x and y directions are denoted as u and δ, respectively. Obviously, δ is a function of u. The updated profile function of the left asperity during climbing can be expressed as

$$y_L = -b\sqrt{1-\frac{(x-u)^2}{a^2}} + t + \delta(u) \tag{7}$$

Substituting Eq. (7) into Eqs. (4) and (5), the abscissa of the contact point and the vertical displacement can be obtained as a functions of u as

$$\begin{cases} x_c = \dfrac{x_0+u}{2} \\ \delta(u) = 2b\sqrt{1-\left(\dfrac{x_0-u}{2a}\right)^2} - t \end{cases} \tag{8}$$

The slope of the tangent line to the asperity profile at the contact point can be determined as

$$k = \tan\theta = \frac{dy_R}{dx}\Big|_{x=x_c} = \frac{b(x_0-u)}{2a^2\sqrt{1-\left(\frac{x_0-u}{2a}\right)^2}} \tag{9}$$

with the local unit tangent vector

$$(\tau_x, \tau_y) = \left(\frac{1}{\sqrt{k^2+1}}, \frac{k}{\sqrt{k^2+1}}\right) \tag{10}$$

The interaction forces in the normal and tangential directions, with magnitudes denoted as T_n and T_τ, respectively, and directions shown in Fig. 2c and d, are assumed to follow Coulomb's law,

$$T_\tau = fT_n, \tag{11}$$

where f denotes the friction coefficient. Their resultant projections along the coordinate directions x and y can be written as

$$\begin{cases} F_x = T_n \cdot \tau_y + T_\tau \cdot \tau_x \\ F_y = T_n \cdot \tau_x - T_\tau \cdot \tau_y \end{cases} \tag{12}$$

Note that, in the above kinematic analyses, the mineral platelets and asperities are regarded as rigid at this stage of modeling. In the following sections, we will include the effects of elastic deformation as well as the constraint from outside the RVE.

2.1. Constraints from surrounding materials

In general, the upper and lower edges of the RVE in Fig. 1d are not free but constrained by surrounding materials and the far-field stress from external loading, especially considering that some seashells live in deep sea where the hydrostatic pressure is high. As shown in Figs. 1d and 3a, the constraints from surrounding materials can be modeled as a layer of elastic cushion with stiffness K_c. Note that the cushion layer can be assumed to have a thickness of unit length, and K_c has a dimension of stress/length and can be determined by classic theoretical models of inclusions, e.g., self-consistent method (Kanaun and Levin, 2008), or adjusted as a varying parameter to investigate the influence of different external constraints (e.g., far-field hydrostatic pressure from living environment). Additionally, the biopolymer connecting adjacent platelets provides tensile forces that resists interface opening due to asperity climbing. Both the platelets and asperities are expected to undergo deformation due to contact interactions. At an arbitrary instant of asperity climbing, we can assume that the asperity height and platelet thickness are reduced by δ_a and δ_p, respectively (Fig. 2e), while the tensile elongation of biopolymer bands is denoted as δ_b and the compression of the effective cushion layer as δ_c. For simplicity, we do not consider the non-uniform deformation due to local contact forces at this point, but will include this effect later using a coefficient of modification.

Taking the right asperity for example, the reduction of height can be estimated under the assumption of uniaxial compression:

$$\delta_a(u) = \int_0^b \frac{F_y dy}{E_p A_R(y)} = \frac{F_y}{E_p} \int_0^b \frac{dy}{A_R(y)} \tag{13}$$

where $A_R(y) = 2a\sqrt{1-(y/b)^2}$ is the cross-sectional area function of asperity along the y-axis and $\int_0^b 1/A_R(y)dy$ is a constant for a specific design of asperity, and F_y is the component of contact force in the y direction, as defined in Eq. (12).

The tensile force in the biopolymer band can be written as

$$F_b = 2lE_b\delta_b(u)/t \tag{14}$$

where l represents the band length; see Fig. 3a. The force exerted by the effective cushion layer of surrounding constraint can be calculated as

$$F_c = 2(a+d)K_c\delta_c(u) = 2(a+d)E_p\varepsilon_p = 2(a+d)E_p\delta_p(u)/D \tag{15}$$

The equilibrium of a mineral platelet in the y direction demands (see Fig. 3b)

$$F_y = F_c + F_b \tag{16}$$

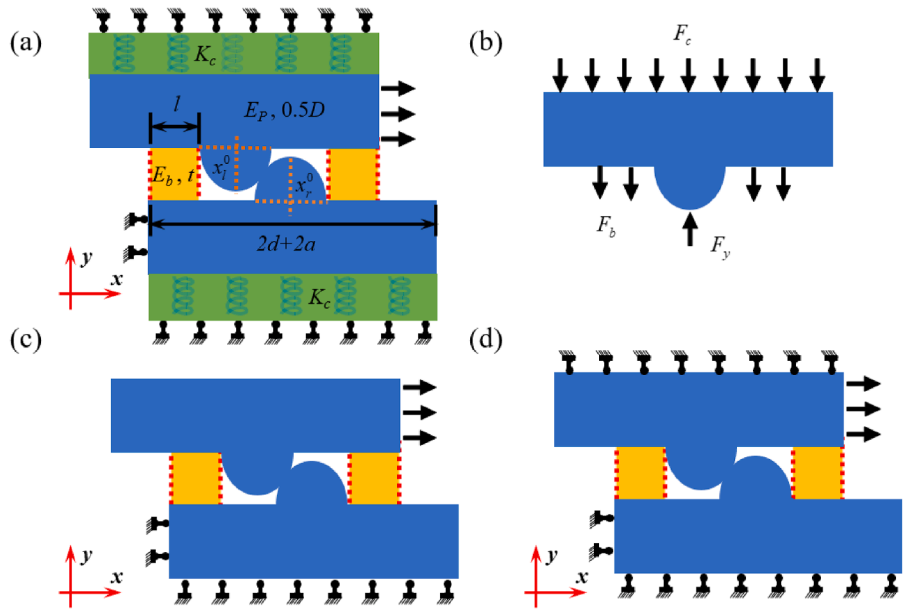

Fig. 3. Illustrations of different constraint conditions from the upper and lower surrounding materials: (a) The constraint modeled as an elastic cushion layer with a finite stiffness; (b) the force balance of a hard platelet along the y direction; (c) the extremely weak constraint modeled as a free boundary condition; and (d) the extremely strong constraint modeled as a fixed boundary condition in the y direction.

and the displacements must satisfy the following kinematic equations

$$\begin{cases} 2\delta_a(u) + \delta_b(u) = \delta(u) \\ \delta_p(u) + 2\delta_c(u) - \delta_b(u) = 0 \end{cases} \tag{17}$$

Solving Eqs. (13-17) yields

$$\begin{cases} 2\delta_a(u) = f_1\delta_p(u) + f_2\delta_b(u) \\ \delta_p(u) = \left[(1+f_2)(1+2f_3) + f_1\right]^{-1}\delta(u) \\ \delta_b(u) = (1+2f_3)\delta_p(u) = \left(\delta(u) - f_1\delta_p(u)\right)/(1+f_2) \end{cases} \tag{18}$$

in which

$$\begin{cases} f_1 = \pi b(a+d)/(aD) \\ f_2 = \pi blE_b/(atE_p) \\ f_3 = (E_p/D)/K_c \end{cases} \tag{19}$$

where f_1 and f_2 correlate δ_a with δ_p and δ_b, respectively, and f_3 is the stiffness ratio of the platelet to the effective cushion layer.

Combining Eqs. (12)-(18), the asperity interaction forces F_y and F_x can be obtained as

$$\begin{cases} F_y = 2(a+d)\dfrac{E_p}{D}\left[(1+f_2)(1+2f_3) + f_1\right]^{-1}\delta(u) + 2l\dfrac{E_b}{t}\left[(1+f_2) + f_1/(1+2f_3)\right]^{-1}\delta(u) \\ F_x = \dfrac{f\cdot n_x + n_y}{n_x - f\cdot n_y}F_y \end{cases} \tag{20}$$

In the expression of F_y, the first term denotes the contribution from the platelet compression under the cushion layer constraint while the second term is from the biopolymer-band tension.

In the above analysis, the compressive strain (stress) in the mineral platelet segment of length $2(a+d)$ is assumed to be uniform, without considering the asymmetric and local effects of the inclined contact force. To account for these effects, two modifications are necessary. First, a coefficient η is introduced to modify the resultant force by the platelet compression, characterizing the asymmetric influence of the inclined contact force during asperity inter-climbing. Hence, Eq. (20) is reformatted as

$$\begin{cases} F_y = (2a+\eta d)\dfrac{E_p}{D}\left[(1+f_2)(1+2f_3) + f_1\right]^{-1}\delta(u) + 2l\dfrac{E_b}{t}\left[(1+f_2) + f_1/(1+2f_3)\right]^{-1}\delta(u) \\ F_x = \dfrac{f\cdot n_x + n_y}{n_x - f\cdot n_y}F_y \end{cases} \tag{21}$$

where

$$\eta = (K_c + 2E_P/D)/(K_c + E_P/D) \tag{22}$$

The asymmetric influence is mainly dominated by the ratio of platelet lateral stiffness over cushion layer stiffness, E_p/DK_c. For the extremely strong constraint (i.e., $K_c = \infty$), only the rear side (opposite to the contact side) is under compression (see Fig. A.1 in Appendix A), in which case η should be nearly 1. For the extremely weak constraint (i.e., $K_c = 0$), the asymmetric effect is negligible, and η can be taken to be 2. One can refer to Appendix A for more detailed discussions. Generally, K_c should be between the two limits, dependent on the surrounding materials as well as the far-field external loadings; if the far-field loading conditions are not considered, its intrinsic value can be determined by classic theoretical models of inclusions, e.g., self-consistent method. For example, with geometrical and material parameters from nacre (Jackson et al. 1988; Dashkovskiy et al. 2007; Meyers et al. 2008), K_c is 0.23 GPa/nm determined by the self-consistent method. Considering the local effect of the contact force, according to the theory of elasticity (Timoshenko and Goodierwrited 1970), the effect of contact on mineral platelet becomes quite weak when the distance from an asperity goes beyond $5a$ (see Appendix B for details). Thus, the following modification about d is applied,

$$d = \min\{d, 5a\} \tag{23}$$

2.2. Weak constraint from surrounding materials

In the limit of extremely weak constraint, the upper and lower boundaries can be regarded as completely free (as shown in Fig. 3c), i.e., $F_c = 0$, and Eq. (16) reduces to

$$F_y = F_b \tag{24}$$

Since the stiffness of the cushion layer $K_c = 0$, $f_3 = \infty$. Thus, the compression deformation of the hard platelet $\delta_p = 0$, and the tensile elongation of biopolymer bands δ_b can be derived according to Eq. (18):

$$\delta_b(u) = \delta(u)/(1+f_2) \tag{25}$$

Finally, the interaction forces F_y and F_x can be obtained according to Eqs. (12) and (14):

$$\begin{cases} F_y = 2l\dfrac{E_b}{t}(1+f_2)^{-1}\delta(u) \\ F_x = \dfrac{f\cdot\tau_x+\tau_y}{\tau_x - f\cdot\tau_y}F_y \end{cases} \tag{26}$$

2.3. Strong constraint from surrounding materials

In the limit of extremely strong constraint, the upper and lower boundaries can be regarded as completely fixed in the y direction (as shown in Fig. 3d). In this scenario, the stiffness of the cushion layers K_c tends to be infinity and $f_3 = 0$. The rigid displacement $\delta(u)$ caused by the asperity climbing leads to an elastic compressive deformation of the adjacent mineral platelets (as shown in Fig. 3d). Therefore, Eq. (18) can be rewritten as

$$\begin{cases} \delta_p(u) = (1+f_2+f_1)^{-1}\delta(u) \\ \delta_b(u) = \delta_p(u) = \big(\delta(u) - f_1\delta_p(u)\big)/(1+f_2) \end{cases} \tag{27}$$

The interaction forces F_y and F_x can be rewritten as

$$\begin{cases} F_y = (2a+\eta d)\dfrac{E_p}{D}(1+f_2+f_1)^{-1}\delta(u) + 2l\dfrac{E_b}{t}(1+f_2+f_1)^{-1}\delta(u) \\ F_x = \dfrac{f\cdot\tau_x+\tau_y}{\tau_x - f\cdot\tau_y}F_y \end{cases} \tag{28}$$

In particular, the platelet modulus E_p is far (about three orders of magnitude) greater than the biopolymer modulus E_b, and so the tensile force F_b generated by the elongation of biopolymer bands and f_2 can be ignored. Hence, Eq. (16) reduces to

$$F_y = F_c \tag{29}$$

and correspondingly, Eq. (28) can be simplified as

$$\begin{cases} F_y = (2a+\eta d)\dfrac{E_p}{D}(1+f_1)^{-1}\delta(u) \\ F_x = \dfrac{f\cdot\tau_x+\tau_y}{\tau_x - f\cdot\tau_y}F_y \end{cases} \tag{30}$$

2.4. Transverse displacement analysis

In the transverse direction (along the x-axis), the relative displacement between two mineral asperities in contact can be divided into two parts: one is the rigid relative displacement u, and the other arises from the transverse bending of the asperities under contact forces (as shown in Fig. 2f). Taking the right asperity as an example, we apply simple bending theory for a cantilever beam with variable cross-section to estimate the maximum transverse deflection of the asperity, which can be expressed as

$$\Delta_a = \int_0^b \int_0^y \frac{M(y)}{E_p I(y)}\,dydy \tag{31}$$

Here, the moment is estimated as $M(y) = F_x\cdot(b-y)$ and the second moment of cross-section area $I = \frac{1}{12}\left(2a\sqrt{\left(1-\frac{y^2}{b^2}\right)}\right)^3$ for the half-ellipse profile of asperity. Consequently, the transverse deflection can be derived as

$$\Delta_a = \frac{1.5b^3F_x(2-\pi/2)}{a^3E_P} \tag{32}$$

The total transverse displacement between the pair of contacting asperities is

$$\Delta = u + 2\,\Delta_a \tag{33}$$

With the transverse force F_x and displacement Δ derived for the pair, we can obtain the complete traction-separation curve to characterize their interaction during inter-climbing. Furthermore, the effective shear stress and strain can be defined as follows:

$$\tau = \frac{F_x}{2a} \tag{34}$$

$$\gamma = \frac{\Delta}{t} \tag{35}$$

leading to an effective interfacial modulus:

$$G = \frac{\tau}{\gamma} \tag{36}$$

Finally, an effective cohesive law ($\tau \sim \Delta$ plot) has been established to model the interaction of mineral asperities. This cohesive law can be implemented into finite element (FEM) or bar-spring models (Xie et al. 2019; Geng et al. 2020) to analyze the behaviors of different forms of mineral asperities and their roles in overall strengthening and toughening mechanisms of nacre and nacre-like composites.

3. Results and discussion

3.1. Cohesive law for elliptical asperities

Based on the derivations in the previous section, cohesive laws for elliptical asperities are presented and discussed in this section. For validation purposes, FEM simulations were conducted and results compared to theoretical predictions. Fig. 4a shows an example of the FEM model, in which the vertical displacement (in the y direction) was constrained at the top and bottom boundaries and periodic boundary conditions applied along the vertical edges. Displacement loading in the x direction was imposed on the right edge of the upper part while the left edge of the lower part fixed. The elastic modulus and Poisson's ratio of platelet material were set to be $E_p = 100$ GPa and $\nu_p = 0.3$, respectively. Other parameters include friction coefficient taken to be $f = 0.3$, platelet thickness $D = 40$ nm, interface thickness $t = 2$ nm, span and height of asperity $2a = 3$ nm and $b = 1.25$ nm. The spacing between neighboring asperities d was

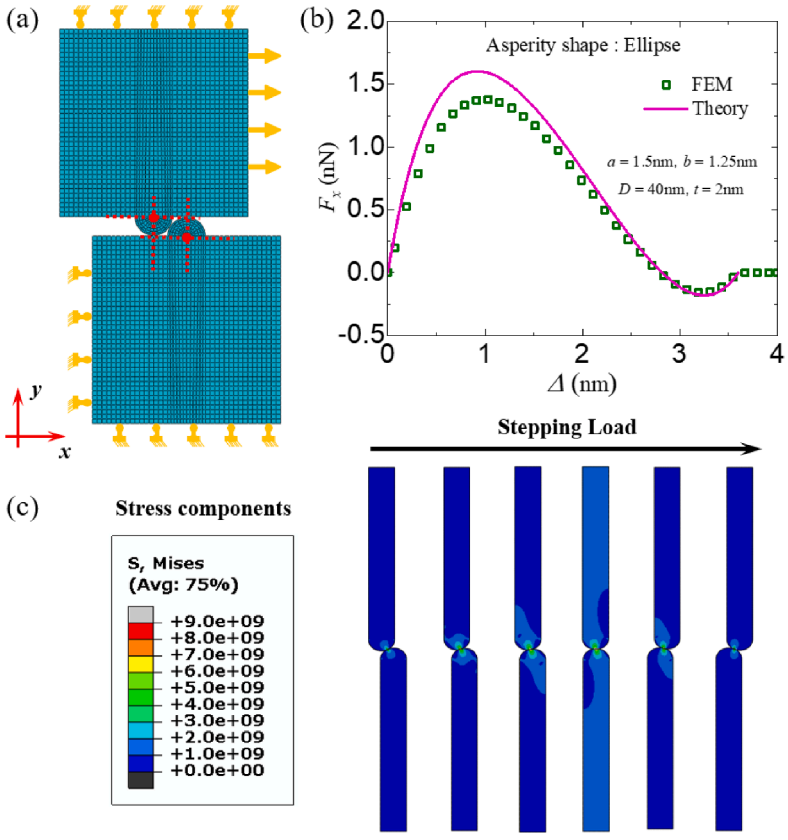

Fig. 4. Validation of the theoretical model of contact and climbing interactions between a pair of elliptical asperities with finite element simulations: (a) FEM model setup, (b) traction-separation plots from theory and FEM, and (c) evolution of stress contours during the climbing process.

considered a variable in the study. The element CPS4R in ABAQUS was adopted, with size around 0.1 nm. The mesh convergence analysis was conducted to guarantee consistent and reliable simulation results. In line with the theoretical model, the separation Δ corresponds to the relative displacement between the centers (see the dots in Fig. 4a) of two contacting asperities in the FEM simulations.

Fig. 4b shows the traction-separation curve during asperity climbing. As the asperities climb against each other, the traction force gradually increases and reaches a peak value. Then, it starts to gradually decrease across zero and reaches a negative minimum value before rising again and finally resting at zero at the end of climbing. Eq. (21) shows that the traction force is determined by two factors: the vertical compressive force and the unit tangent vector. Their variations during the climbing process govern how the traction varies with displacement. Negative traction corresponds to unstable downhill sliding, meaning that the upper asperity would spontaneously slide down the lower one if not under the constraint of horizontal displacement. Note that the peak traction force in Fig. 4b is slightly larger than the FEM result, because our homogenization-based analyses on asperity compressive deformation by Eq. (13) overlooks the localized deformation due to stress concentration, and hence gives a slight underestimation on the height reduction of asperities, consequently a slight overestimation on the interaction forces between contacted asperities. Fig. 4c shows the evolution of stress contours in the pair of contacting asperities during the climbing process. In the strong constraint scenario, one can see that the compressive stress in the mineral platelet is asymmetric, as only the rear side (opposite to the contact side) of each asperity is under compression.

To investigate the effect of spacing d between adjacent asperities, the variations of traction stress versus separation for different d are plotted in Fig. 5 under the condition of extremely strong constraints on the top and bottom boundaries. As the spacing d/a increases from 0 to 5, one can see that the magnitude of traction stress gradually increases. This trend is reasonable since the platelet compressive strain/stress due to the asperity climbing is basically independent of d and remains almost constant in this region. Therefore, a larger platelet length would lead to a larger compressive force F_y, and consequently a larger traction force F_x according to Eq. (30). However, as d/a increases beyond 5, the $\tau \sim \Delta$ plots change more slowly and exhibit a trend to converge. The FEM results are in good agreement with our theoretical argument in Eq. (23) (see Appendix B for details). Generally speaking, Fig. 5 shows that our theoretical model agrees well with the simulation results by FEM.

To demonstrate the effect of elastic constraint from the surrounding materials, the traction-separation curves predicted by our theoretical model, along with the FEM results, are presented in Fig. 6 for different cushion-layer stiffness values. It can be seen that the theoretical predictions align closely with the FEM results. As expected, the traction stress goes up with the increase in cushion-layer stiffness. Note our theoretical models for the strong and weak boundary constraints represent the upper and lower limits, thereby bounding the curves under elastic boundary conditions. In Fig. 6, one can also observe that the traction-separation curve has approached the upper limit when the cushion-layer stiffness K_c reaches 4E5 GPa/nm in the simulation setup. In the weak constraint boundary condition, the Young's modulus of the biopolymer bands E_b was set to be 200 MPa.

3.2. Cohesive law for the asperities of different shapes

In natural biological materials or bioinspired synthetic composites, the shape of mineral asperities can take different profiles. Thus, it is of practical interest to investigate the influence of asperity shape on the cohesive behaviors of nacre-like interfaces. We considered four common shapes for a comparative analysis: ellipse, hyperbolic cosine, cosine, and parabola. The theoretical derivations for the latter three shapes are quite similar to that for the elliptical shape, and the detailed derivations can be found in Appendix C. The theoretical traction-separation curves for the strong and weak constraint boundary conditions are shown in Figs. 7 and 8, respectively, along with the corresponding FEM simulations for validation purposes. In these examples, we set the platelet volume fraction $\phi = 0.95$, the inter-asperity spacing $d = 4a$, and the asperity aspect ratio to vary from 0.6 to 0.9. One can observe that the theoretical predictions are in good agreement with the FEM results. Different asperity shapes generally provide similar cohesive behaviors in the two limiting

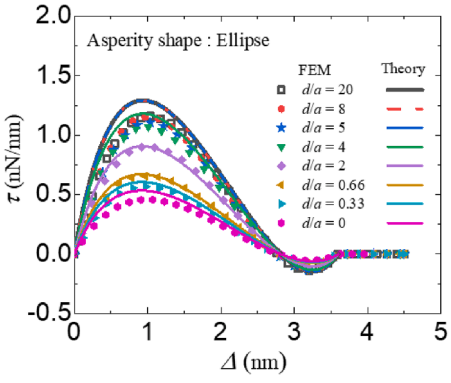

Fig. 5. Effect of asperity spacing d on the traction-separation curves.

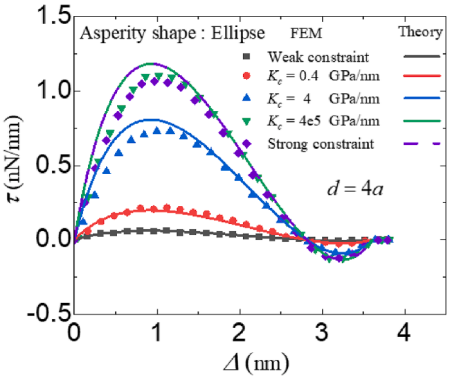

Fig. 6. Effect of constraint from the surrounding of RVE on the traction-separation curve: A larger stiffness K_c of the elastic cushion layer indicates stronger constraint; the weak and strong constraints correspond to the free and fixed boundaries, respectively.

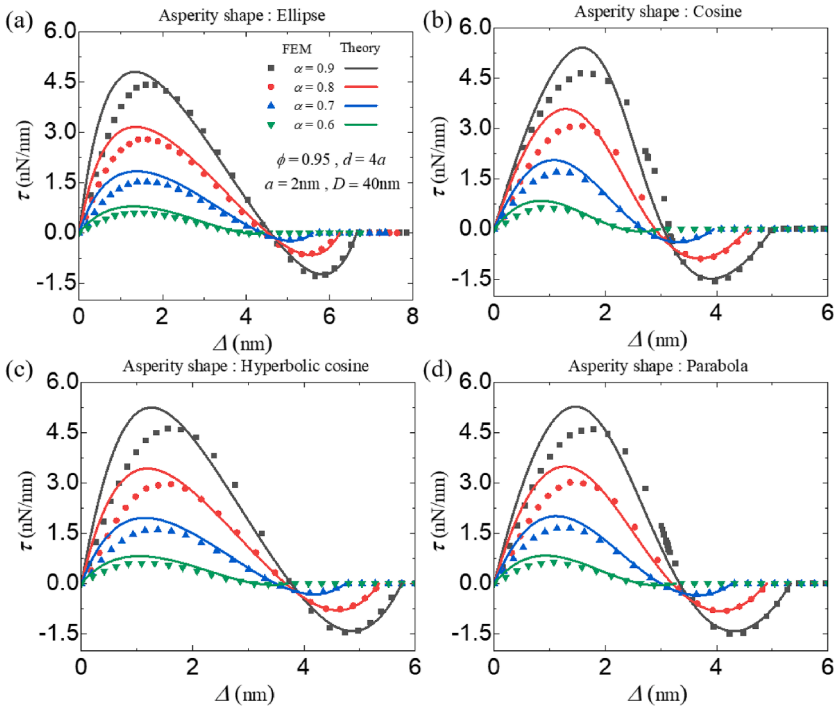

Fig. 7. Theoretical predictions of traction-separation curves for different asperity shape profiles under fixed (extremely strong constraint) boundary conditions: (a) ellipse, (b) parabola, (c) hyperbolic cosine, and (d) cosine. Here $\phi = 0.95$, $d = 4a$, and the aspect ratio varies from 0.6 to 0.9. FEM results are included for comparison purposes.

scenarios, and the traction shows a similar varying trend with respect to displacement, and the peak traction always increases with increasing asperity aspect ratio. The magnitudes of the peak stresses are at the same level, except that it is slightly smaller with the elliptical shape under the weak constraint boundary condition. For all asperity shapes under consideration, the peak traction under the weak constraint is generally an order of magnitude less than that under the strong constraint. Furthermore, the top peaks show a significant shift to the right with the cosine and parabola profiles, especially when the aspect ratio is large and the boundary constraint strong; see Fig. 7b and d. The peak-shift-to-right phenomenon is mainly due to the transverse bending deformation of asperities (see Eq. (32) in Section 2.4). Among the example asperity shapes considered here, the cosine and parabola shapes are tall and thin while the

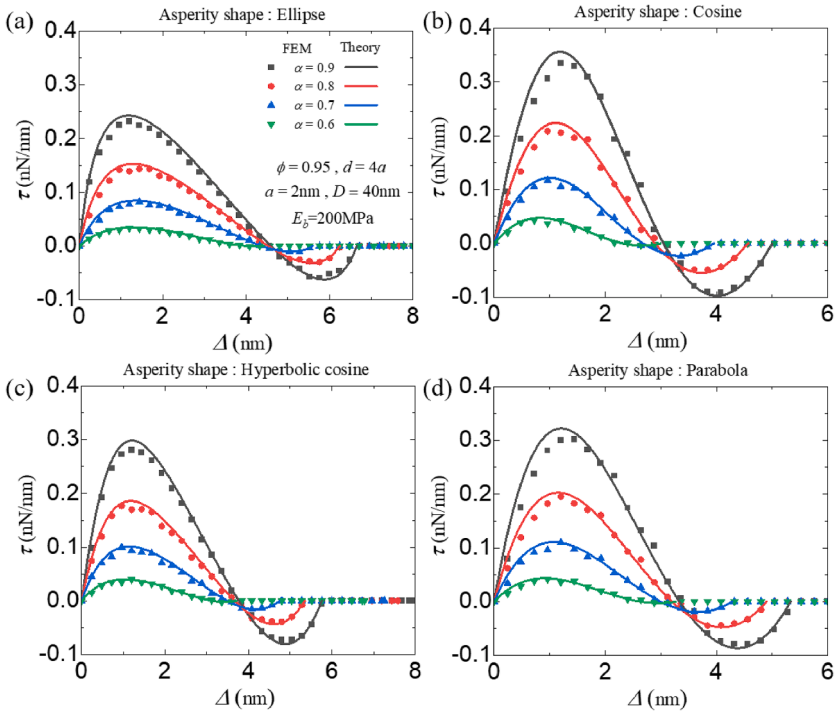

Fig. 8. Theoretical predictions of traction-separation curves for different asperity shape profiles under free (extremely weak constraint) boundary conditions: (a) ellipse, (b) parabola, (c) hyperbolic cosine, and (d) cosine. $\phi = 0.95$, $d = 4a$, and the aspect ratio varies from 0.6 to 0.9. FEM results are included for comparison purposes.

elliptical and hyperbolic cosine shapes are relatively short and fat. The asperities with taller-and-thinner shape profiles have smaller bending stiffnesses and stronger constraints provide larger contact forces, leading to more significant transverse bending deformations and resulting in a peak-shift-to-right behavior in the traction-separation curves. In contrast, the transverse bending deformation and peak-shift-to-right behavior are negligible under weak constraint since the contact force is relatively small.

From the comparison among different asperity shapes, it is interesting to observe that the asperity shape only has a marginal influence on the interfacial cohesive behaviors, whereas the asperity aspect ratio has a much more significant influence. This indicates that the asperity aspect ratio (i.e., ratio of roughness height over width) is a critical design parameter to tune mechanical properties of the interface, while the effect of asperity shape is marginal. This finding may serve as useful and practical guidelines for the design and implementation of nacre-inspired roughness. In addition, one may notice that, in Fig. 7, the peak traction forces given by our theoretical model are slightly larger than the FEM results, while their corresponding separations are slightly smaller than the FEM results. The former deviation is mainly due to our homogenization-based modeling on the asperity compressive deformation (see Eq. (13)), as discussed before about Fig. 4b. Similarly, the origin of the latter deviation lies in our homogenization-based modeling on the asperity bending deformation (see Eq. (31)), in which the localized deformation induced by stress concentration is not taken into consideration, so that the asperity transverse deflection Δ_a and further the total lateral displacement Δ are slightly underestimated. The effects of localized deformation would be especially distinct under the strong constraint boundary conditions (as adopted in Figs. 4 and 7), since the interaction forces between contacted asperities are large and the stress concentration effects are strong. To the contrary, we can see in Fig. 8 that the deviations between our theoretical predictions and FEM results become trivial when the free (weak constraint) boundary conditions are adopted.

3.3. *Geometrical influences on the cohesive properties*

Based on the traction-separation curve, the equivalent interface modulus, strength, and work-to-fracture (under the stress-strain curve area) are defined as the secant slope from the origin to the peak, the maximum traction, and the area under the curve, respectively. The three mechanical indices can be used to reflect the stiffening, strengthening, and toughening contributions of mineral asperities to the composites. By analyzing the varying trends of these parameters with respect to the geometrical parameters of asperities, we can quantitatively investigate the geometrical influences on the cohesive behaviors of rough interface.

Fig. 9 shows the effective interface modulus, strength, and work-to-fracture varying with the asperity aspect ratio for the four asperity shapes: ellipse, cosine, hyperbolic cosine, and parabola. Here both the upper limit of strong constraint and lower limit of weak constraint are considered, with an asperity spacing $d = 4a$. In these examples, no asperity aspect ratios less than 0.5 are considered, as an aspect ratio of 0.5 corresponds to the case where the upper and lower asperities just slide over each other's tip without mutual

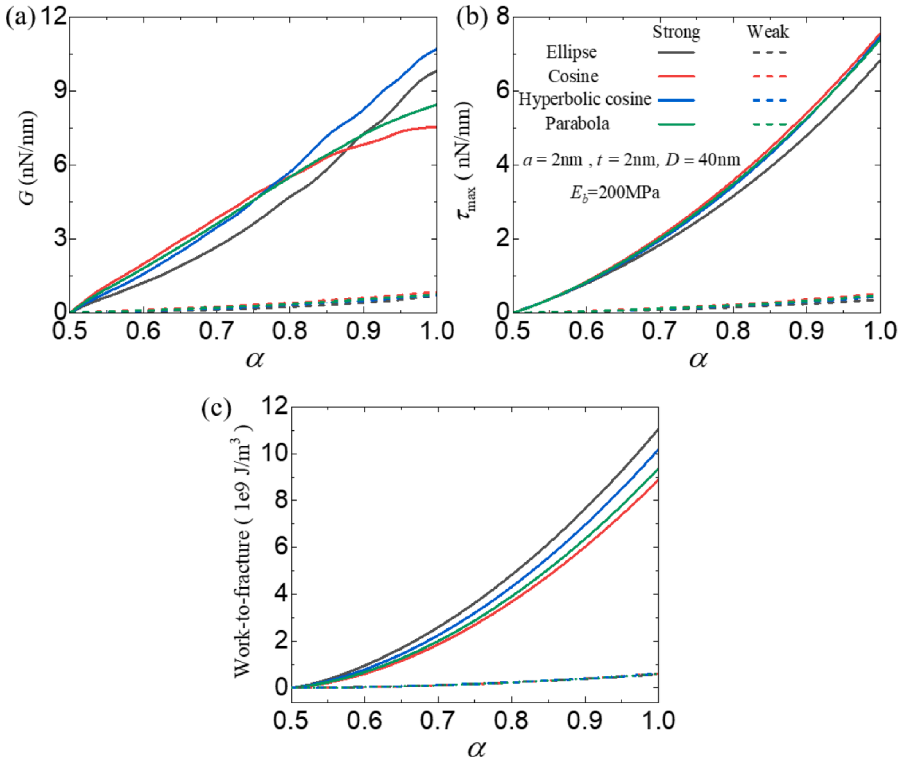

Fig. 9. Plots of the effective interfacial mechanical properties under fixed (strong constraint) and free (weak constraint) boundary conditions with respect to the aspect ratio α of mineral asperity for the typical profiles of ellipse, cosine, hyperbolic cosine, and parabola: (a) Modulus, (b) Strength, and (c) Work-to-fracture. Here the mineral volume fraction ϕ has been set to 0.95.

compression. From Fig. 9, one can observe that the mechanical properties generally increase with increasing asperity aspect ratio. The difference among the four asperity shapes is not significant, which is consistent with the observations made in Section 3.2. As the asperity aspect ratio approaches 1, the interface modulus and strength under the strong constraint are approximately an order of magnitude larger than those under the weak constraint, while the interfacial work-to-fracture is about two orders of magnitude larger. This suggests that the compressive constraints from the surrounding material are critical for the asperities to manifest their stiffening, strengthening, and toughening roles. However, it is important to note that the polymer bands alone are insufficient to resist the interfacial expansion caused by asperity inter-climbing, resulting in inadequate interaction forces between pairs of contacting asperities. Additionally, under the strong constraint condition, the interface moduli of the cosine and parabola-shaped asperities become smaller than those of the elliptical and hyperbolic cosine-shaped asperities, and tend to saturate when the asperity aspect ratio exceeds 0.85. This behavior can be attributed to the aforementioned peak-shift-to-right phenomenon in the traction-separation curves of tall and thin-shaped profiles (e.g., the cosine and parabola shapes) due to transverse bending deformation of the asperities (see Fig. 7b and d). It is worth pointing out that beyond a critical value of the asperity aspect ratio, the interfacial properties cannot continue to increase, as the material yielding and failure would come into effect. However, the plastic yielding and failure behaviors are not taken into account in the present model for simplicity, especially considering that the nanoscale mineral materials have extremely high strengths, close to their theoretical limits (Gao et al. 2003; Danzer et al. 2013; Alghamdi et al. 2018).

The volume fraction of reinforcements is an important design parameter for composites, and thus the influence of platelet volume fraction is investigated. Eq. (2) suggests that the platelet volume ratio is positively correlated with the ratio D/t. Here we keep the asperity dimension (width a and aspect ratio α) and interface thickness t fixed, and obtain different platelet volume ratios by varying the platelet thickness D. Nacre-like composites usually have relatively large reinforcement volume fraction, and so a range of platelet volume ratios from 0.80 to 0.98 are considered. Fig. 10 presents the effective interface modulus, strength, and work-to-fracture varying with respect to the volume fraction, including both the fixed and free boundary constraints. As the platelet volume fraction increases, all three interface properties gradually decrease in the strong constraint scenario. The trend is easily understood with Eq. (30), which indicates that the traction force F_x and hence the stress τ would decrease as the platelet thickness D increases while t is held constant. The underlying mechanism is that the elastic platelet acts as a cushion layer between the interface and rigid boundary, and hence a

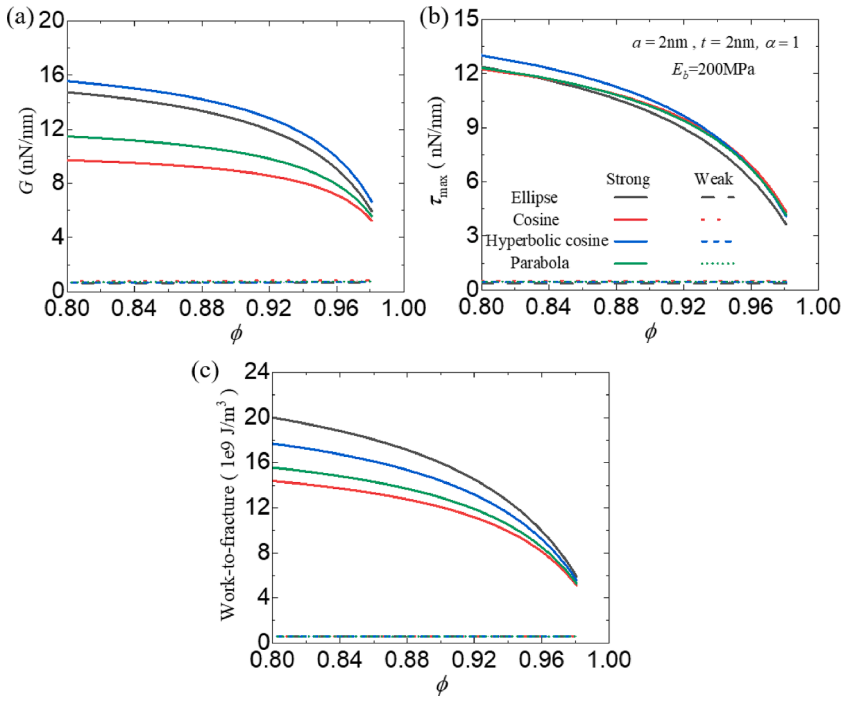

Fig. 10. Plots of the effective interface properties under different boundary conditions with respect to the mineral volume fraction ϕ for the common asperity profiles of ellipse, cosine, exponential, and parabola: (a) Interface Modulus, (b) Strength, and (c) Work-to-fracture. Here the aspect ratio of mineral asperity α is set to 1.

thicker platelet would accommodate a larger portion of the asperity-climbing induced interfacial expansion through its own deformation, finally leading to a smaller contact force between contacting asperities. If the volume ratio is approaching 1, the interface asperity would effectively vanish, and the interface interaction would become a plane-to-plane contact with friction. In the weak constraint scenario, the effective interface modulus, strength, and work-to-fracture remain low and independent of the volume fraction. The result is expected since Eq. (26) suggests that in the weak constraint situation, the contact forces are only related to the geometrical parameters of the interface and asperity (i.e., *a, b, l*, and *t*), not to the platelet thickness *D*. In fact, the interface is a self-equilibrated and self-determined system in the extremely weak constraint boundary condition considered in this study.

3.4. Mechanical behaviors of platelets sliding with multiple asperities

In the previous sections, we have focused on the cohesive law corresponding to a single pair of mineral asperities on the interfaces of nacre-like composites. In practice, nacre and nacre-like composites contain multiple asperities on their interfaces, as shown in Fig. 1b and c. To study the effects of multiple asperities, we implemented the derived cohesive law of a single pair of asperities into a multiple-asperity interface model. Fig. 11 illustrates the adopted methodology. A representative unit cell in Fig. 1c is modeled as a bar-spring system, as shown in Fig. 11a. The platelets and asperity pairs are modeled as bars and discrete springs, respectively. The bars are assigned the material properties of mineral platelets, while the springs are assigned the traction-separation law derived from the single pair of inter-climbing asperities in the previous sections, as shown in Fig. 11b. As the neighboring mineral platelets slide relative to each other, an asperity that climbs over one of its contacting neighbors may move forward, meet the next neighbor, and restart the climbing process. To simulate this process, a spring broken at one spot can be reformed at another once the asperity contact reoccurs, as illustrated in Fig. 11a. The equilibrium analysis of an element is shown in the inset of Fig. 11a. The effective spring constant is determined by $k_{12}^{q} = G(\Delta)/t$, in which the instantaneous effective interface modulus $G(\Delta)$, defined as the secant slope, can be obtained from the traction-separation law, as presented in Fig. 11b. Note that, as shown in Fig. 11b, the instantaneous modulus is set to zero (i.e., the spring is considered to be broken) when the traction falls to zero or below at the end of an inter-climbing process. At this stage, downhill sliding of the asperity happens spontaneously and makes no contributions to stiffening, strengthening and toughening. Fig. 11c shows the flowchart for determining the curve of tensile force versus elongation as the overlapping platelets slide over and off

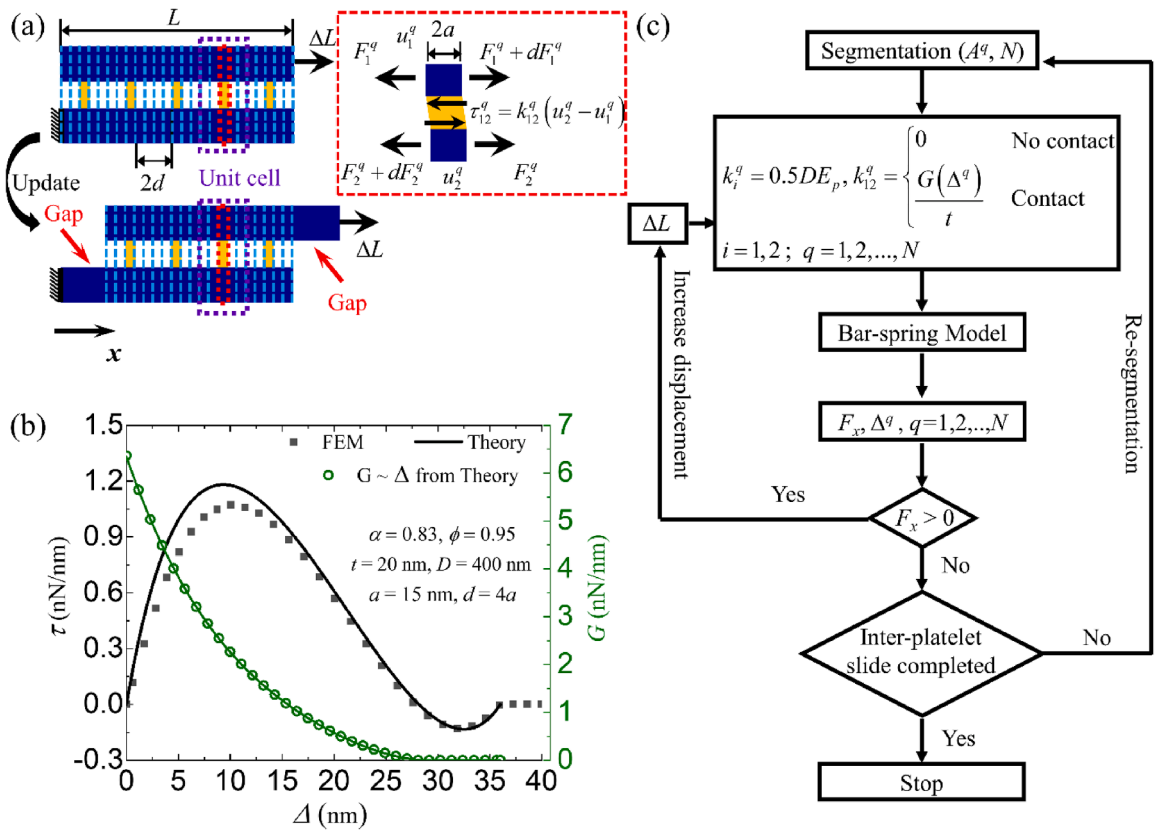

Fig. 11. Incorporating the asperity climbing model as a cohesive law into the "bar-spring" model of sliding between multiple-asperity mineral platelets in nacre-like composites: (a) schematic of the "bar-spring" model for a typical RVE of nacre's brick-and-mortar structure, (b) example cohesive law for the "spring" given by the theoretical model of a pair of interacting asperities, and (c) computational flow-chart simulating the inter-platelet sliding. For simplicity, other components such as biopolymer and mineral bridges are ignored on purpose.

each other. The calculation is done using our previously developed Floquet-based bar-spring model (Xie et al. 2019; Geng et al. 2020). Noteworthy that the cohesive law can also be directly and easily implemented into common commercial FEM software such as ABAQUS, as material behavior input of cohesive elements.

For completeness, we briefly introduce the basic equations of the Floquet-based bar spring model. For detailed information, one can refer to our previous papers (Xie et al. 2019; Geng et al. 2020). Without loss of generality, the governing equations for an arbitrary segment – say the q-th segment - are

$$\tau_{12}^q = k_{12}^q(u_2^q - u_1^q) \tag{37}$$

$$\begin{cases} \dfrac{\mathrm{d}F_1^q}{\mathrm{d}x} = k_{12}^q(u_1^q - u_2^q) \\ \dfrac{\mathrm{d}F_2^q}{\mathrm{d}x} = k_{12}^q(u_2^q - u_1^q) \end{cases} \tag{38}$$

$$\begin{cases} \dfrac{\mathrm{d}u_1^q}{\mathrm{d}x} = \dfrac{F_1^q}{k_1^q} \\ \dfrac{\mathrm{d}u_2^q}{\mathrm{d}x} = \dfrac{F_2^q}{k_2^q} \end{cases} \tag{39}$$

where $q = 1,\ldots, N$, with N denoting the total number of segments, $x \in [x_{q-1},\ x_q]$ and $k_1^q = k_2^q = 0.5D \cdot E_p$ is the bar/platelet tensile stiffness. Introduce a column vector $\boldsymbol{\xi} = (F_1, u_1, F_2, u_2)^{\mathrm{T}}$, and rewrite the system of equations in a matrix form

$$\frac{\mathrm{d}\boldsymbol{\xi}}{\mathrm{d}x} = \mathbf{A}_q\boldsymbol{\xi} \tag{40}$$

where $\mathbf{A}_q$ is a 4th-order constant matrix

$$A_q = \begin{bmatrix} 0 & k_{12}^q & 0 & -k_{12}^q \\ \frac{1}{k_1^q} & 0 & 0 & 0 \\ 0 & -k_{12}^q & 0 & k_{12}^q \\ 0 & 0 & \frac{1}{k_2^q} & 0 \end{bmatrix} \tag{41}$$

The Floquet-based bar-spring model amounts to establishing the relation

$$\boldsymbol{\xi}(x_q) = e^{\mathbf{A}_q l_q} \boldsymbol{\xi}(x_{q-1}) \tag{42}$$

Through a recursive derivation, the forces and displacements at the two end boundaries are connected by the following equation

$$\begin{bmatrix} F_1(L) \\ u_1(L) \\ F_2(L) \\ u_2(L) \end{bmatrix} = \prod_{q=1}^{N} (\nabla) e^{\mathbf{A}_q l_q} \begin{bmatrix} F_1(0) \\ u_1(0) \\ F_2(0) \\ u_2(0) \end{bmatrix} \tag{43}$$

in which (∇) indicates that the product is ordered with respect to decreasing q, l_q is the length of the q-th segment, L is the total length of the representative unit cell. As shown in Fig. 11a, applying a displacement loading ΔL, the following four boundary conditions are known,

$$\begin{cases} u_1(L) = \Delta L \\ u_2(0) = 0 \\ F_1(0) = 0 \\ F_2(L) = 0 \end{cases} \tag{44}$$

and the other four boundary quantities $u_1(0), u_2(L), F_1(L), F_2(0)$ can be solved from Eq. (43). Once all boundary conditions are fully determined, we can insert them into Eq. (42) to obtain the tensile forces, displacements, and shear stress in every segment recursively.

To verify the bar-spring model, the calculated results are compared to those from FEM simulations, as shown in Figs. 12a and b for the strong and weak constraint situations, respectively. In the example, the platelet length $L = 150$ nm, half-thickness $0.5D = 20$ nm, and the interface thickness $t = 2$ nm. The elliptical shape was adopted for the asperities, with span $2a = 3$ nm and height $b = 1.25$ nm. Ten asperities were evenly distributed along the interface with spacing of $2d = 12$ nm. The elastic modulus, Poisson's ratio, and friction coefficient of the platelet material were set to E_p= 100 GPa, $\nu_p = 0.3$, and $f = 0.3$, respectively. In the weak constraint situation, an ideal elastoplastic material model was adopted for the biopolymer matrix, with typical parameters of Young's modulus E_b=200 MPa and yield stress σ_b^y=20 MPa. As shown in Fig. 12, our model predictions agree well with the FEM simulation results for both the strong and weak constraint boundary conditions. This agreement validates the use of our bar-spring model and cohesive law. Interestingly, the plots of tensile force versus elongation exhibit a multimodal feature, with ten gradually decreasing peaks corresponding to the successive sliding over the ten asperities. Notably, the maximum force produced by the strong constraint condition is dramatically larger than that by the weak constraint condition.

According to previous studies on natural nacre (Wang et al. 2001; Barthelat et al. 2006; Katti and Katti 2006; Espinosa et al. 2009; Alghamdi et al. 2018), the hard platelets in nacre have a length of about 4.05 μm and a thickness of about 400 nm. The interface thickness between adjacent platelets is approximately 20 nm. The asperities on the interface have a width of about 30 nm, a height of about 12.5 nm, and are spaced $2d$=420 nm apart, corresponding to an asperity density of 2–3/μm^2 (Song et al. 2003; Alghamdi et al.

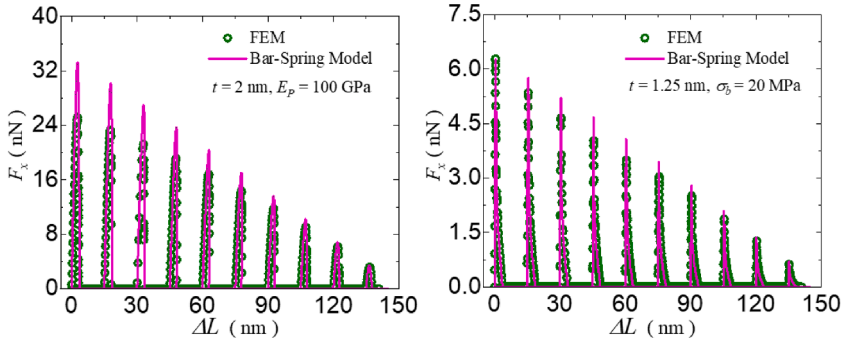

Fig. 12. Comparison of the bar-spring model predictions with FEM simulation results of sliding between 10-asperity mineral platelets in a nacre-like composite: the force-displacement curves under strong (a) and weak constraint boundary conditions (b).

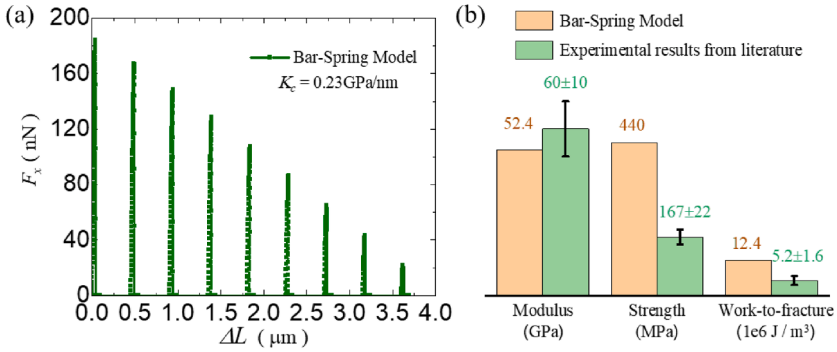

Fig. 13. Mechanical properties of composite close to nacre: (a) Force-displacement curve, and (b) Comparison of predicted effective properties with experimental results from the literatures (Jackson et al. 1988; Jackson et al. 1990; Alghamdi et al. 2020).

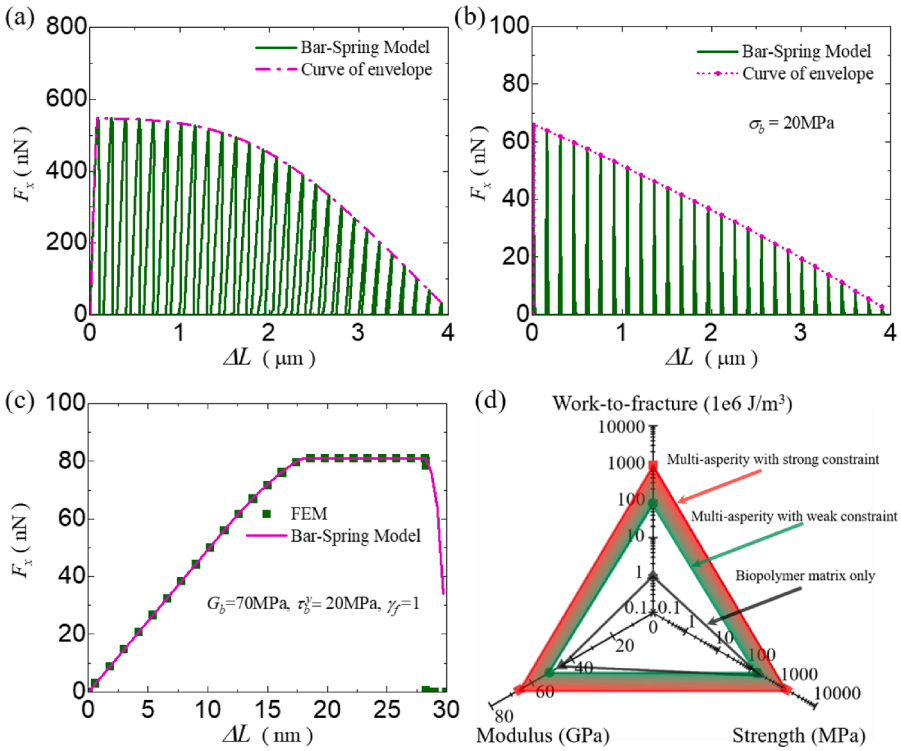

Fig. 14. Mechanical properties of nacre-like composite with multi-asperity mineral platelets: Force-displacement plot under strong constraint (a), weak constraint (b), and biopolymer matrix without asperities (c); the simultaneous enhancements in stiffness, strength and toughness by the nacre-inspired multi-asperity designs (d).

2018). We assume that the nano-asperities are evenly distributed, with 9 asperities on each mineral platelet. The volume fraction of mineral ϕ =0.95 (Meyers et al. 2008) and the modulus of mineral platelet E_p = 100 GPa (Jackson et al. 1988; Jackson et al. 1990; Dashkovskiy et al. 2007) are adopted, and correspondingly K_c = 0.23 GPa/nm is determined by the self-consistent method. With these geometrical and material parameters, our bar-spring model is applied to a representative unit cell of nacre, and gives the force-displacement curves as shown in Fig. 13a. The effective modulus, strength, and work-to-fracture can be determined, respectively, as the initial slope, the maximum stress, and the under-the-curve area. Fig. 13b shows a comparison between our predictions and experimental results from the literatures in the composite's effective modulus, strength, and work-to-fracture (Jackson et al. 1988; Jackson et al. 1990). Our model predicted an effective modulus of nacre 52.4 GPa, agreeing with the experimental result in the range of 50–70 GPa (Jackson et al. 1988; Jackson et al. 1990). The predicted strength and work-to-fracture are 440 MPa and 12.4E6 J/m^3, respectively, while the experimental results are 155–189 MPa (Jackson et al. 1988) and 3.6E6–6.8E6 J/m^3 (Alghamdi et al. 2020), respectively. The slight overestimations in the strengthening and toughening effects of asperities may result from two aspects: 1) our model is two dimensional with the asperities existing continuously along the third dimension, and 2) no yielding and damage within

the mineral platelets and asperities were considered in our model. To verify our analyses, an additional calculation modeling the mineral asperities as bumps (with a finite length along the third dimension) was conducted, and the results are shown in Appendix D. One can see that the agreement between our theoretical predictions and the experimental results is greatly improved.

One important objective of studying natural biological materials such as nacre is to help develop synthetic materials of high performance. To this end, we show an example of nacre-inspired composite design to demonstrate the stiffening, strengthening and toughening effects of multi-asperity interface. In the example, 27 asperities are introduced on each mineral platelet, spaced $2d = 120$ nm apart and evenly distributed. The force-displacement curves are shown in Fig. 14a and b, respectively, for the case of strong and weak constraint. As the peak number/density in the force-displacement curves increases with the asperity number/density, the force would move from peak to peak as the displacement increases under practical loading scenarios, resulting in the apparent force-displacement relations that appear as envelopes in Fig. 14a and b. Comparing Fig. 14a with Fig. 11b, one can estimate that the maximum force is enlarged by an order of magnitude due to the synergistic effort of multiple asperities. In order to make a comparison, the corresponding model with only biopolymer matrix filling the interface was also simulated by our bar-spring model as well as FEM. In this case, an ideal elastoplastic material model is adopted for the biopolymer matrix, with typical parameters of Young's modulus $E_b = 200$ MPa, Poisson's ratio $\nu_b = 0.45$, yield stressτ_b^y=20 MPa, and a failure strainγ_f=1. The force-displacement curve presented in Fig. 14c clearly shows the deformation stages of elasticity, plasticity and ultimate failure with increased displacement loading. Fig. 14d shows a comparison among the three cases (i.e., the strong constraint, the weak constraint, and the biopolymer matrix only) in the effective modulus, strength, and work-to-fracture (the under-curve area of envelopes). As expected, the strong constraint provides distinctly superior mechanical properties over the weak constraint, with about an order of magnitude rise in the effective strength and toughness. The two extreme constraint situations serve as the upper and lower bound estimations of asperity contribution to the mechanical properties, and show plenty of space (area between the two bounds in Fig. 14d) for tuning the composite properties through interface roughness design. The comparison among the three cases under the same two-dimensional model clearly shows the undisputed effects of mineral asperities in stiffening, strengthening, and toughening. Regarding the composite's modulus and strength, the biopolymer only case shows comparable performance to the rough interface design under extremely weak constraint but much poorer than the rough interface case under strong constraint. In terms of the work-to-fracture, the rough interface designs can yield two to three orders of magnitude higher performance than the biopolymer only design. This is mainly attributed to the astonishingly enlarged length scale of interface interactions by the successive inter-asperity climbing process - from the characteristic failure length of biopolymers around several nanometers to the whole interface length of overlapping platelets around several micrometers.

4. Summary

Nacre is primarily composed of stiff and brittle mineral platelets, constituting over 95% of its volume. Despite this, it manages to achieve remarkable and well-balanced mechanical properties, including stiffness, strength, and toughness. Within the sub-microscale structure of nacre, the presence of mineral asperities at the inter-platelet interfaces has been speculated to play a pivotal role. With an aim to better understand the stiffening, strengthening, and toughening effects of the mineral asperities, our current work established a micromechanical model based on the kinematic and deformation analysis of a single pair of contacting asperities, where an effective cohesive law was derived to characterize the traction-separation relationship during asperity inter-climbing. Subsequently, the cohesive law was seamlessly integrated into a Floquet-based bar-spring model. This hierarchical model is simple and computationally efficient, allowing for the simulation of overlapped platelets with multiple asperities sliding over each other in nacre or nacre-like composites. Finally, we obtained the complete tensile force versus elongation curves of nacre-like composites, from which the effective mechanical properties of the composites—such as modulus, strength and work-to-fracture—were determined.

With this approach of hierarchical modeling, the interface properties, including shear modulus, strength, and toughness for various asperity designs, were analytically derived; a range of influence factors, such as asperity spacing, shape, and aspect ratio, were systematically examined; their effects on the stiffening, strengthening, and toughening of nacre-like composites were also demonstrated. Specifically, the key findings and conclusions below are worth being highlighted:

(1) The micromechanical model developed here provides a cohesive law for convenient applications in the studies of nacre and nacre-inspired composites, which effectively captures the interactions between a pair of contacting and inter-climbing mineral asperities, as well as their contributions in the stiffening, strengthening and toughening mechanisms of composites. The model was validated by comparing theoretical predictions with FEM simulations results.
(2) Interfacial asperities play indispensable roles in the stiffening, strengthening, and toughening of nacre and nacre-like composites. In comparison to the smooth interfaces filled only with biopolymers, a rough interface with multiple asperities can elevate the composites' strength to almost an order of magnitude, and toughness by two to three orders in magnitude. Such enhancement in mechanical performance is mainly attributed to the mechanical interlocking and multimodal friction-like characteristics of the inter-climbing process among multiple asperities in the interface.
(3) Rough interfaces with designed asperities were shown to be a robust strategy to stiffen, strengthen, and toughen nacre-like composites of practical interest since their effects are insensitive to the asperity shapes, such as ellipse, hyperbolic cosine, cosine, and parabola studies here. This facilitates the design and fabrication of bioinspired interfaces in the practical engineering of composites.

(4) The asperity aspect ratio and density (asperity number per unit length of interface, related to their width and spacing) exhibit distinct influences on the enhancement effects in stiffness, strength, and toughness. Hence, these parameters can effectively serve as tunable variables of design to acquire desired mechanical properties of nacre-inspired synthetic composites.

It is worth noting that the theoretical model developed here is intended for nacre and nacre-like composites, in which submicroscale asperities as parts of the hard reinforcements usually have quite high elastic modulus with comparison to the soft matrices so that the hard contact and inter-climbing behavior should be dominant in the interactions among asperities during the reinforcement platelets sliding against one another. The model can be easily extended to a more general scenario where the asperities consist of a different material from that of reinforcements, just by introducing the asperity modulus as an independent material variable. However, the elastic modulus of asperities cannot be very small; otherwise, severe localization of deformation in the contact region of asperities will occur, the asperities will be flattened and slide over each other without the need for climbing over, and thus our theoretical model here is no longer applicable. The exclusion of possible material yielding and failure is another limitation of our present model. Further work is also needed to address these issues in the future. Moreover, nacre, as a hierarchical biological material, has multiple structural features and correspondingly complicate mechanical behaviors across several length scales. The strengthening and toughening mechanisms related to every structure features and their synergistic effects are yet to be explored by researchers in this field.

CRediT authorship contribution statement

Hao Li: Writing – original draft, Validation, Software, Investigation, Data curation. **Kun Geng:** Validation, Software, Formal analysis. **Bingzhan Zhu:** Validation, Software. **Qiang Zhang:** Validation, Software. **Yi Wen:** Software, Formal analysis. **Zuoqi Zhang:** Writing – review & editing, Writing – original draft, Visualization, Validation, Supervision, Software, Resources, Project administration, Methodology, Investigation, Funding acquisition, Formal analysis, Data curation, Conceptualization. **Yanan Yuan:** Writing – review & editing, Writing – original draft, Project administration, Methodology, Funding acquisition, Conceptualization. **Huajian Gao:** Writing – review & editing, Writing – original draft, Visualization, Methodology, Funding acquisition, Conceptualization.

Declaration of competing interest

The authors declare that they have no known competing financial interests or personal relationships that could have appeared to influence the work reported in this paper.

Data availability

Data will be made available on request.

Acknowledgments

The work was supported by National Natural Science Foundation of China (Grant Nos. 12272279, 11720101002, 11772240, 12372138, 12002244) and Key R&D Plan Projects of Hubei Province (No. 2021BCA106). H. G. also acknowledges funding support from the Ministry of Education in Singapore under grant MOE-MOET32022–0002.

Appendixes

A. *Asymmetric effect of the contact force*

In the case of extremely weak constraint, the contact force is small, and the platelet surfaces can be assumed to remain horizontal during the inter-climbing process. Thus, the compressive strain (stress) in the y direction of the mineral platelet is nearly uniform, and the resultant compressive force in the segment of length $2a + 2d$ can be expressed as Eq. (15)

$$F_c = (2a + 2d)E_p\delta_p(u) \,/\, D \tag{A.1}$$

However, this is not the case when the constraint from surrounding materials is strong and the contact force large, because the contact occurs only on one side and the resultant force is inclined, as shown in Fig. 2. To illustrate this point more clearly, we performed FEM simulations to check stress distributions in the mineral platelets under the extremely strong constraint condition. The compressive stress contour is shown in Fig. A.1. One can clearly see that the compressive stress distribution is asymmetric and non-uniform. The stress distribution as well as the stress level (~1 GPa in order of magnitude) agrees well with the previous studies in the literature (Barthelat et al. 2006; Alghamdi et al. 2018). The compressive stress only appears in the rear side, and hence the resultant compressive force would reduce to

$$F_c = (2a + d)E_p\delta_p(u) \,/\, D \tag{A.2}$$

Analysis shows that the compressive stress distribution in the mineral platelets should be related to the ratio of the platelet stiffness in the y direction over the cushion layer stiffness, i.e., E_p/DK_c. When the stiffness ratio is extremely large, it can be expected that the resultant compressive force approximates Eq. (A.1). On the contrary, it would become close to Eq. (A.2) when the stiffness ratio is extremely small. Between the two limits, a smooth transition is hypothesized as follows,

$$F_c = (2a+\eta d)E_p\delta_p(u) \,/\, D \tag{A.3}$$

$$\eta = \frac{K_c + 2E_P/D}{K_c + E_P/D} \tag{A.4}$$

B. Local effect of the contact force

For a semi-infinite space subjected to a uniform pressure p on a region of length $2a$ on its surface, as shown in Fig. B.1a, the classic theory of elasticity gives the stress field as follows,

$$\begin{cases} \sigma_{xx} = \dfrac{-2}{\pi}\displaystyle\int_{-a}^{a} \frac{qy(x-\xi)^2 d\xi}{\left(y^2+(x-\xi)^2\right)^2} \\ \sigma_{yy} = \dfrac{-2}{\pi}\displaystyle\int_{-a}^{a} \frac{qy^3 d\xi}{\left(y^2+(x-\xi)^2\right)^2} \\ \tau_{xy} = \dfrac{-2}{\pi}\displaystyle\int_{-a}^{a} \frac{qy^2(x-\xi) d\xi}{\left(y^2+(x-\xi)^2\right)^2} \end{cases} \tag{B.1}$$

It can be inferred that the magnitudes of stresses decrease away from the loading center. Specifically, Fig. B.1b shows that the stress component σ_{yy} decreases with increasing r, and one can see that it has decayed to less than 20% of the pressure p when r is beyond $6a$.

For an asperity with width $2a$, the pressure on the asperity base region (with a length of $2a$) due to the inter-asperity contact can be assumed uniform with a magnitude p, analogous to Fig. B.1a. Then, the compressive stress in the mineral platelet around the asperity would be similar to that shown in Fig. B.1b. One can conclude that the compressive stress in the mineral platelet becomes negligible beyond a critical distance r_c=$6a$. If the half inter-asperity spacing d is no larger than $5a$, then the whole unit cell is within the range of r_c and the length $2(a+d)$ should be adopted to calculate the resultant compressive force in the platelet, as Eq. (15) shows. Otherwise, a part of the platelet is out of the range of r_c and has trivial contribution to the resultant compressive force, and $2r_c$=$2\times 6a$=$12a$ will be used to calculate the resultant compressive force. Hence, the following modification of d should be made to consider the local effect of the asperity contact,

$$d = \begin{cases} d & d \le 5a \\ 5a & d > 5a \end{cases} = \min\{d, 5a\} \tag{B.2}$$

C. Theoretical model derivation for different shaped asperities

In the main text, our model was focused on elliptical-shaped asperities. In principle, it can be extended to other asperity shapes with ease. For comparison purposes, here several asperity shapes such as parabola, hyperbolic cosine, and cosine are considered. The basic derivation steps are similar to those for the elliptical shape, and thus only some key equations are shown here. Corresponding to Eq. (3), the profile functions for the other three asperity shapes are expressed in Table C.1, while the abscissas (x_0) of the right asperity center are presented in Table C.2.

Corresponding to Eq. (8), the elevating displacement during the inter-climbing process can be obtained, as summarized in Table C.3. Corresponding to Eq. (9), the slope of the tangent line to the asperity profile at the contact point is shown in Table C.4.

The dimensionless parameters f_1 and f_2 in Eq. (19) are derived, as listed in Table C.5.

To analyze the transverse displacement due to the asperity bending [see Eq. (31)], the second moments of cross-sectional area for different asperities are determined, as shown in Table C.6. It is worth noting that the cross-section width in the asperity shapes of hyperbolic cosine and cosine was approximately taken as the first two terms of their Taylor expansion for simplicity.

Corresponding to Eq. (32), the transverse deflection can be derived and listed in Table C.7.

D. Additional calculation with the mineral asperities modeled as bumps

The theoretical predictions for nacre show a noticeable deviation from the experimental measurements in the literature, see Fig. 13b. We infer that the deviations are partly because the asperities are modeled as ridges in our 2D model whereas they are more

like bumps in nacre. To validate this point, here a modified version of our model is developed, in which the mineral asperities were modeled as bumps (with a finite length along the out-of-plane direction, e.g., half of the out-of-plane thickness of mineral platelets) instead of the ridges. The new results are presented in Fig. D.1, with comparison to the experimental results and those predicted by the original ridge-asperity model. We can observe that much better agreement between the theoretical predictions and experimental results is obtained.

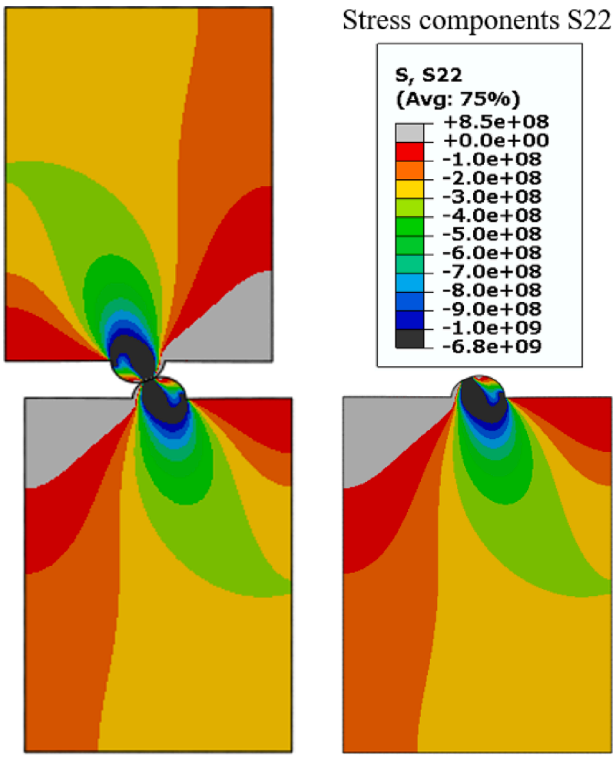

Fig. A.1. Stress contour of S22 with extremely strong constraint.

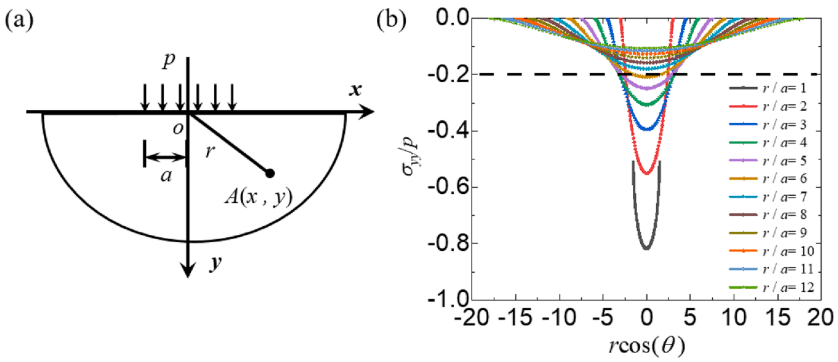

Fig. B.1. Schematic diagram of semi-infinite space subjected to uniform pressure on a part of surface (a) and the stress component σ_{yy} decaying with increasing distance r from the origin point O (b).

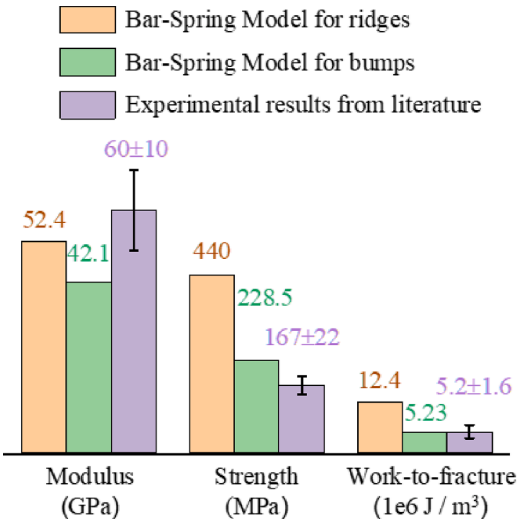

Fig. D.1. The predicted effective properties of nacre by the bump-asperity model, with comparison to the experimental results and those predicted by the ridge-asperity model.

Table C.1
Profile functions of different shaped asperities.

Shape function	y_l	y_r
Parabola	$\frac{b}{a^2}x^2$	$\frac{b}{a^2}\left(2a^2-(x-x_0)^2\right)-t$
Hyperbolic cosine	$\frac{b}{e^{wa}+e^{-wa}-2}(e^{wx}+e^{-wx})$	$\frac{b}{e^a+e^{-a}-2}(2(e^a+e^{-a})-(e^{(x-x_0)}+e^{-(x-x_0)}))-t$
Cosine	$-b\cos\left(\frac{\pi x}{2a}\right)+t$	$b\cos\left(\frac{\pi(x-x_0)}{2a}\right)$

Table C.2
The abscissas x_0 of the right asperity center.

Shape function	x_0
Parabola	$x_0=\sqrt{\frac{2(2b-t)}{b/a^2}}$
Hyperbolic cosine	$x_0=2\ln\left(1+\frac{2b-t+\sqrt{8(b/(e^a+e^{-a}-2))(2b-t)+(2b-t)^2}}{4b/(e^a+e^{-a}-2)}\right)$
Cosine	$x_0=\frac{4a}{\pi}\arccos\left(\frac{t}{2b}\right)$

Table C.3
The elevating displacement $\delta(u)$.

Shape function	$\delta(u)\sim u$
Parabola	$\delta(u)=-\frac{b}{2a^2}(u-x_0)^2+2b-t$
Hyperbolic cosine	$\delta(u)=\frac{2b}{e^a+e^{-a}-2}\left((e^a+e^{-a})-\left(e^{\left(\frac{x_0-u}{2}\right)}+e^{-\left(\frac{x_0-u}{2}\right)}\right)\right)-t$
Cosine	$\delta(u)=2b\cos\left(\frac{\pi}{4a}(x_0-u)\right)-t$

Table C.4
the slope k of the tangent line at the contact point.

Shape function	k
Parabola	$k=\frac{b}{a^2}(x_0-u)$
Hyperbolic cosine	$k=\frac{b}{e^a+e^{-a}-2}\left(e^{\left(\frac{x_0-u}{2}\right)}-e^{-\left(\frac{x_0-u}{2}\right)}\right)$
Cosine	$k=\frac{b\pi}{2a}\sin\left(\frac{\pi}{4a}(x_0-u)\right)$

Table C.5
The dimensionless parameters f_1 and f_2.

Shape function	f_1 , f_2
Parabola	$f_1 = 4b(a+d)/(aD)$, $f_2 = 4blE_b/(atE_p)$
Hyperbolic cosine	$f_1 = 4b(a+d)/(aD)$, $f_2 = 4blE_b/(atE_p)$
Cosine	$f_1 = \sqrt{2}b\pi(a+d)/(aD)$, $f_2 = \sqrt{2}blE_b/(atE_p)$

Table C.6
The second moment of cross-sectional area.

Shape function	I
Parabola	$I = \frac{1}{12}\left(\frac{2\sqrt{b-y}}{\sqrt{b/a^2}}\right)^3$
Hyperbolic cosine	$I = \frac{1}{12}\left(2\sqrt{\frac{b-y}{b/(e^a+e^{-a}-2)}}\right)^3$
Cosine	$I = \frac{1}{12}\left(\frac{2\sqrt{2-2\frac{y}{b}}}{\pi/2a}\right)^3$

Table C.7
The transverse deflection of asperities.

Shape function	Δ_a
Parabola	$\Delta_a = (b/a)^3 F_x/E_P$
Hyperbolic cosine	$\Delta_a = \left(\frac{b^2}{e^a+e^{-a}-2}\right)^{3/2} F_x/E_P$
Cosine	$\Delta_a = 0.25\sqrt{2}b^3(\pi/2a)^3 F_x/E_P$

References

Alghamdi, S., Du, F., Yang, J., Pinder, G., Tan, T., 2020. Tensile and shear behavior of microscale growth layers between nacre in red abalone. J. Mech. Phys. Solids. 138, 103928.

Alghamdi, S., Du, F., Yang, J., Tan, T., 2018. The role of water in the initial sliding of nacreous tablets: findings from the torsional fracture of dry and hydrated nacre. J. Mech. Behav. Biomed. Mater. 88, 322–329.

Alghamdi, S., Tan, T., Hale-Sills, C., Vilmont, F., Xia, T., Yang, J., Huston, D., Dewoolkar, M., 2017. Catastrophic failure of nacre under pure shear stresses of torsion. Sci. Rep. 7 (1), 13123.

Bar-On, B., Wagner, H.D., 2011. Mechanical model for staggered bio-structure. J. Mech. Phys. Solids. 59 (9), 1685–1701.

Barthelat, F., 2007. Biomimetics for next generation materials. Philos. Trans. a Math. Phys. Eng. Sci. 365 (1861), 2907–2919.

Barthelat, F., Espinosa, H.D., 2007. An Experimental Investigation of Deformation and Fracture of Nacre–Mother of Pearl. Exp. Mech. 47 (3), 311–324.

Barthelat, F., Li, C.-M., Comi, C., Espinosa, H.D., 2006. Mechanical properties of nacre constituents and their impact on mechanical performance. J. Mater. Res. 21 (8), 1977–1986.

Checa, A.G., Cartwright, J.H., Willinger, M.G., 2011. Mineral bridges in nacre. J. Struct. Biol. 176 (3), 330–339.

Chen, Y., Ma, Y., Yin, Q., Pan, F., Cui, C., Zhang, Z., Liu, B., 2021. Advances in mechanics of hierarchical composite materials. Compos. Sci. Technol. 214.

Chen, Y., Wang, S., Liu, B., Zhang, J., 2015. Effects of geometrical and mechanical properties of fiber and matrix on composite fracture toughness. Compos. Struct. 122, 496–506.

Chen, Y.L., Liu, B., He, X.Q., Huang, Y., Hwang, K.C., 2010. Failure analysis and the optimal toughness design of carbon nanotube-reinforced composites. Compos. Sci. Technol. 70 (9), 1360–1367.

Currey, J.D., Sheppard, P.M., 1977. Mechanical properties of mother of pearl in tension. In: Proceedings of the Royal Society of London. Series B. Biological Sciences, 196, pp. 443–463.

Danzer, R., Lube, T., Morrell, R., Supancic, P., 2013. Mechanical Properties of Ceramics. Handbook of Advanced Ceramics, 2nd Ed. Wileys.

Dashkovskiy, S., Suhr, B., Tushtev, K., Grathwohl, G., 2007. Nacre properties in the elastic range: influence of matrix incompressibility. Comput. Mater. Sci. 41 (1), 96–106.

Doineau, E., Cathala, B., Benezet, J.C., Bras, J., Le Moigne, N., 2021. Development of bio-inspired hierarchical fibres to tailor the fibre/matrix interphase in (bio) composites. Polymers. (Basel) (5), 13.

Espinosa, H.D., Rim, J.E., Barthelat, F., Buehler, M.J., 2009. Merger of structure and material in nacre and bone – Perspectives on de novo biomimetic materials. Prog. Mater. Sci. 54 (8), 1059–1100.

Evans, A.G., Suo, Z., Wang, R.Z., Aksay, I.A., He, M.Y., Hutchinson, J.W., 2001. Model for the robust mechanical behavior of nacre. J. Mater. Res. 16 (9), 2475–2484.

Gao, H., 2006. Application of fracture mechanics concepts to hierarchical biomechanics of bone and bone-like materials. Int. J. Fract. 138 (1–4), 101–137.

Gao, H.J., Ji, B.H., Jager, I.L., Arzt, E., Fratzl, P., 2003. Materials become insensitive to flaws at nanoscale: lessons from nature. Proc. Natl. Acad. Sci. u S. a 100 (10), 5597–5600.

Geng, K., Xie, W., Chen, B., Yin, Q., Yuan, Y., Zhang, Z., 2020. Failure simulation and design optimization of bioinspired heterogeneous interfaces by Floquet-based bar-spring model. Compos. Struct. 252, 112665.

Ghazlan, A., Ngo, T.D., Tran, P., 2015. Influence of interfacial geometry on the energy absorption capacity and load sharing mechanisms of nacreous composite shells. Compos. Struct. 132, 299–309.

Jackson, A.P., Vincent, J.F.V., Turner, R.M., 1988. The mechanical design of nacre. Proc. R. Soc. Lond. Ser. B 234, 415–440.

Jackson, A.P., Vincent, J.F.V., Turner, R.M., 1990. Comparison of Nacre with Other Ceramic Composites. J. Mater. Sci. 25 (7), 3173–3178.
Jager, I., Fratzl, P., 2000. Mineralized collagen fibrils: a mechanical model with a staggered arrangement of mineral particles. Biophys. J. 79 (4), 1737–1746.
Ji, B., Gao, H., 2004. Mechanical properties of nanostructure of biological materials. J. Mech. Phys. Solids. 52 (9), 1963–1990.
Ji, B., Gao, H., Wang, T., 2004. Flow stress of biomorphous metal–matrix composites. Mater. Sci. Eng. 386 (1–2), 435–441.
Kanaun, S., Levin, V., 2008. Self-Consistent Methods for Composites, eighth ed. Springer Netherlands, Berlin.
Katti, K.S., Katti, D.R., 2006. Why is nacre so tough and strong? Mater. Sci. Eng. 26 (8), 1317–1324.
Li, X., Xu, Z.H., Wang, R., 2006. In situ observation of nanograin rotation and deformation in nacre. Nano Lett. 6 (10), 2301–2304.
Liang, S.M., Ji, H.M., Li, X.W., 2020. Thickness-dependent mechanical properties of nacre in Cristaria plicata shell: critical role of interfaces. J. Mater. Sci. Technol. 44, 1–8.
Liu, J., Xu, Y., Yang, H., Liu, Y., Yarlagadda, P.K., Yan, C., 2020. Investigation of failure mechanisms of nacre at macro and nano scales. J. Mech. Behav. Biomed. Mater. 112, 104018.
Mayer, G., 2006. New classes of tough composite materials—lessons from natural rigid biological systems. Mater. Sci. Eng. 26 (8), 1261–1268.
Menig, R., Meyers, M.H., Meyers, M.A., Vecchio, K.S., 2000. Quasi-static and dynamic mechanical response of Haliotis rufescens (abalone) shells. Acta Mater. 48 (9), 2383–2398.
Meyers, M.A., Chen, P.-Y., Lin, A.Y.-M., Seki, Y., 2008. Biological materials: structure and mechanical properties. Prog. Mater. Sci. 53 (1), 1–206.
Meyers, M.A., Lin, A.Y., Chen, P.Y., Muyco, J., 2008. Mechanical strength of abalone nacre: role of the soft organic layer. J. Mech. Behav. Biomed. Mater. 1 (1), 76–85.
Sarikaya, M., Gunnison, K., Yasrebi, M., Aksay, I., 1989. Mechanical property-microstructural relationships in abalone shell. MRS Proc. 174.
Schäffer, T.E., Ionescu-Zanetti, C., Proksch, R., Fritz, M., Walters, D.A., Almqvist, N., Zaremba, C.M., Belcher, A.M., Smith, B.L., Stucky, G.D., Morse, D.E., Hansma, P. K., 1997. Does abalone nacre form by heteroepitaxial nucleation or by growth through mineral bridges? Chem. Mater. 9 (8), 1731–1740.
Shao, Y., Zhao, H.-P., Feng, X.-Q., Gao, H., 2012. Discontinuous crack-bridging model for fracture toughness analysis of nacre. J. Mech. Phys. Solids. 60 (8), 1400–1419.
Song, F., Bai, Y.L., 2003. Effects of nanostructures on the fracture strength of the interfaces in nacre. J. Mater. Res. 18 (8).
Song, F., Soh, A.K., Bai, Y.L., 2003. Structural and mechanical properties of the organic matrix layers of nacre. Biomaterials 24 (20), 3623–3631.
Song, F., Zhou, J., Xu, X., Xu, Y., Bai, Y., 2008. Effect of a negative Poisson ratio in the tension of ceramics. Phys. Rev. Lett. 100 (24), 245502.
Tan, G., Yu, Q., Liu, Z., Wang, X., Zhang, M., Liu, Y., Zhang, Z., Ritchie, R.O., 2021. Compression fatigue properties and damage mechanisms of a bioinspired nacre-like ceramic-polymer composite. Scr. Mater. 203, 114089.
Tang, Z., Kotov, N.A., Magonov, S., Ozturk, B., 2003. Nanostructured artificial nacre. Nat. Mater. 2 (6), 413–418.
Timoshenko, S.P., Goodierwrited, J.N., 1970. Theory of Elasticity.3rd ed, third ed. McGraw-Hill Book Company.
Troncoso, O.P., Torres, F.G., Arroyo, J., Gonzales, K.N., Fernández-García, M., López, D., 2020. Mechanical properties of calcite- and aragonite-based structures by nanoindentation tests. Bioinspired, Biomimetic Nanobiomaterials 9 (2), 112–121.
Wang, R.Z., Suo, Z., Evans, A.G., Yao, N., Aksay, I.A., 2001. Deformation mechanisms in nacre. J. Mater. Res. 16 (9), 2485–2493.
Xia, S., Wang, Z., Chen, H., Fu, W., Wang, J., Li, Z., Jiang, L., 2015. Nanoasperity: structure origin of nacre-inspired nanocomposites. ACS. Nano 9 (2), 2167–2172.
Xie, W., Yuan, Y., Zhang, Z., 2019. A floquet-based bar-spring model for the dynamic modulus of bioinspired composites with arbitrary staggered architectures. J. Appl. Mech. 86 (9).
Xu, Z.-H., Li, X., 2011. Deformation strengthening of biopolymer in nacre. Adv. Funct. Mater. 21 (20), 3883–3888.
Yao, H.B., Ge, J., Mao, L.B., Yan, Y.X., Yu, S.H., 2014. 25th anniversary article: artificial carbonate nanocrystals and layered structural nanocomposites inspired by nacre: synthesis, fabrication and applications. Adv. Mater. 26 (1), 163–187.
Yu, Z., Liu, J., Wei, X., 2020. A general property-structure relationship from crack stability analysis on hybrid staggered composites with elasto-plastic matrices. Compos. Struct. 240, 112071.
Zhang, Q., Li, H., Liu, Y., Zhang, Z., Yuan, Y., 2022. Nacre-inspired topological design tuning the impact resistant behaviors of composite plates. Compos. Struct. 299.
Zhang, Z., Fan, G., Tan, Z., Zhao, H., Xu, Y., Xiong, D., Li, Z., 2021. Towards the strength-ductility synergy of Al2O3/Al composite through the design of roughened interface. Compos. Part B 224, 109251.
Zhang, Z., Zhang, Y.W., Gao, H., 2011. On optimal hierarchy of load-bearing biological materials. Proc. Biol. Sci. 278 (1705), 519–525.
Zhang, Z.Q., Liu, B., Huang, Y., Hwang, K.C., Gao, H., 2010. Mechanical properties of unidirectional nanocomposites with non-uniformly or randomly staggered platelet distribution. J. Mech. Phys. Solids. 58 (10), 1646–1660.